UC Irvine
UC Irvine Previously Published Works

Title

Thermodynamics and Mechanism of the Membrane Permeation of Hv1 Channel Blockers.

Permalink

Journal

The Journal of membrane biology, 254(1)

ISSN

0022-2631

Authors

Lim, Victoria T
Freites, J Alfredo
Tombola, Francesco
et al.

Publication Date

2021-02-01

DOI

10.1007/s00232-020-00149-8

Peer reviewed

Thermodynamics and mechanism of the membrane permeation of Hv1 channel blockers

Victoria T. Lim[†], J. Alfredo Freites[†], Francesco Tombola[‡,¶], Douglas J. Tobias[†,¶]

[†]Department of Chemistry, University of California, Irvine

[‡]Department of Physiology and Biophysics, University of California, Irvine, California 92697, United States

[¶]Chao Family Comprehensive Cancer Center, University of California, Irvine, California 92697, United States

Abstract

The voltage-gated proton channel Hv1 mediates efflux of protons from the cell. Hv1 integrally contributes to various physiological processes including pH homeostasis and the respiratory burst of phagocytes. Inhibition of Hv1 may provide therapeutic avenues for the treatment of inflammatory diseases, breast cancer, and ischemic brain damage. In this work, we investigate two prototypical Hv1 inhibitors, 2-guanidinobenzimidazole (2GBI) and 5-chloro-2-guanidinobenzimidazole (GBIC), from an experimentally screened class of guanidine derivatives. Both compounds block proton conduction by binding the same site located on the intracellular side of the channel. However, when added to the extracellular medium, the compounds strongly differ in their ability to inhibit proton conduction, suggesting substantial differences in membrane permeability. Here, we compute the potential of mean force for each compound to permeate through the membrane using atomistic molecular dynamics simulations with the adaptive biasing force method. Our results rationalize the putative distinction between these two blockers with respect to their abilities to permeate the cellular membrane.
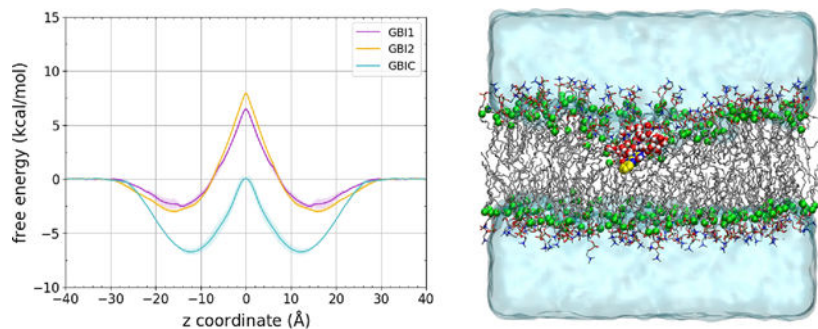
Graphical Abstract

dtobias@uci.edu .

Supporting Information Available

Results and analysis of the pK$_a$ shift profile, as well as a discussion on long timescales for solute flip flop, are presented in the Supporting Information.

Introduction

Hv1 is a voltage-gated proton channel whose primary function is the release of excess protons from the cell.[1–3] Human Hv1 is a homodimer, and each monomer is composed of four transmembrane alpha helices forming the voltage-sensing domain (VSD) which also serves as the proton conduction pathway.[4–10] Hv1 integrally contributes to various physiological processes[1] of which pH homeostasis and respiratory burst in phagocytes are the best characterized.[11–15] Inhibition of Hv1 may provide therapeutic avenues for the treatment of inflammatory diseases,[16–18] breast cancer,[19–22] and ischemic brain damage during stroke.[23–25]

Numerous guanidine derivatives have been found to block proton conduction in the human Hv1 channel by interacting with an intracellular binding site.[26,27] Two molecules in this class, 2-guanidinobenzimidazole (2GBI) and 5-chloro-2-guanidinobenzimidazole (GBIC), rapidly inhibited Hv1-mediated currents when added to the intracellular side of the membrane.[26,27] However, when the compounds were added to the extracellular medium, they displayed very different inhibitory behaviors: GBIC-mediated inhibition slowly reached steady-state within the timescale of the experiment (several minutes), whereas no significant inhibition could be observed with 2GBI over similar periods of time.[27] These observations suggested that external GBIC can cross the membrane and reach the intracellular binding site more effectively than 2GBI.

GBIC differs from 2GBI by the replacement of a hydrogen atom with a chlorine atom on the benzene moiety, and this structural modification may affect the ligand's pharmacokinetic properties. Membrane permeability rates have not been experimentally determined for 2GBI or GBIC, but the permeation process can be examined using molecular simulations. These simulations typically have an advantage over experimental techniques in that they can provide spatially resolved information with atomistic resolution. Molecular dynamics (MD) simulations enable investigation of transport processes at the molecular level to describe and explain important steps including membrane partitioning and molecular flip-flop across the hydrophobic membrane core.[28]

The inhomogeneous solubility-diffusion model[29,30] describes the permeation process derived from the steady-state flux of solute molecules through the membrane.[31] The permeability P_m of some solute to cross a membrane of thickness L is expressed as:

$$\frac{1}{P_m} = \int_{-L/2}^{L/2} \frac{\exp[W(z)/k_B T]}{D(z)} \mathrm{d}z, \tag{1}$$

where $W(z)$ is free energy profile or potential of mean force (PMF) for the translocation of the solute, $D(z)$ is the local diffusion constant of the solute, k_B is the Boltzmann constant, T is the temperature, and z is a collective variable that describes the position of the solute along the transmembrane axis. Our focus in this work is on calculating the PMFs for the translocation of 2GBI and ClGBI across lipid bilayers to gain understanding of their relative permeabilities from a thermodynamic standpoint.

We aimed to investigate the propensity of ClGBI to permeate the lipid bilayer, shedding light on why it may be able to block Hv1 from the extracellular compartment much more efficiently than 2GBI. We employed atomistic MD simulations to compute the potentials of mean force for 2GBI and ClGBI to permeate through a membrane using the adaptive biasing force (ABF) enhanced sampling method,[32,33] which applies a continually updated biasing force to effectively yield a flat free energy surface in the long time limit. ABF has been demonstrated to reproduce experimental membrane permeability trends.[34,35] Our results rationalize the putative distinction between these two blockers on their abilities to permeate the cellular membrane to inhibit Hv1.

Methods

In this work, we compute and examine the one-dimensional potentials of mean force for 2-guanidinobenzimidazole (2GBI) and 5-chloro-2-guanidinobenzimidazole (GBIC) to permeate through a 1-palmitoyl-2-oleoyl-sn-glycero-3-phosphocholine (POPC) bilayer in the direction of the bilayer normal. Chemical structures of the molecules that we study in this work are depicted in Figure 1. For 2GBI, we consider two tautomers, which we refer to as GBI1 and GBI2. Both GBI1 and GBI2 are positively charged but differ in the placement of one hydrogen atom, leading to different regions of partial charge concentration (denoted by the shaded blue regions in Figure 1). These two tautomers were previously investigated in the computation of relative binding free energies to Hv1,[36] and GBI2 was predicted to be the primary tautomeric state that binds to Hv1. In solution of pH 5–8, however, GBI1 may be the more prevalent species as predicted using the ChemAxon pKa plugin (https://docs.chemaxon.com/display/docs/pKa+Plugin). We considered a GBI1-like tautomer of GBIC.

We obtained an initial configuration of a 72-lipid POPC bilayer from the end of a 35 ns simulation at 303 K and 1 atm. This configuration was generated by the group of Jeff Klauda and is available at https://terpconnect.umd.edu/~jbklauda/memb.html. The membrane spanned the xy plane with the z-axis normal to the membrane plane. Using the CHARMM36 force field[37] for the lipid molecules with the modified TIP3P water model,[38,39] we further equilibrated the membrane for 849.6 ns using Desmond 2.4.[40] Short-range realspace interactions were cut off at 12 Å by using a force-based switching function between 8 Å and 12 Å. An r-RESPA algorithm[41] was employed to integrate the equations of motion with a time step of 4 fs for the long-range non-bonded forces, 2 fs for

short-range non-bonded, and 1 fs for bonded forces. The particle mesh Ewald method[42,43] was used to treat long-range electrostatics. All bond lengths involving hydrogen atoms were constrained using SHAKE.[44] The simulation was performed at constant temperature (303 K) and pressure (1 atm), using Nose-Hoover chains[45] and the Martyna-Tobias-Klein barostat.[46]

Given that permeation events may affect membrane structure and to diminish the possibility of boundary effects, we extended the size of the membrane via a 2×2 patch to yield a final system size of 288 POPC molecules (144 per leaflet) and 16,444 water molecules. The cell dimensions were $100 \times 100 \times 90$ Å^3. Simulations with this system were performed using the NAMD 2.13 software package.[47] The system was equilibrated for an additional 20 ns. The temperature was maintained at 295 K using the stochastic velocity rescaling (canonical sampling through velocity rescaling)[48] thermostat with a rescale period of 1 ps and 20 time steps between rescaling. The pressure was maintained at 1 atm using the Nosé-Hoover Langevin piston method[46,49] with an oscillation period of 200 fs and a damping time scale of 100 fs. The O-H bond lengths in water were constrained using the SETTLE algorithm,[50] and all other covalent bonds involving hydrogen atoms were constrained using the RATTLE algorithm.[51] Long-range electrostatic interactions were evaluated using the particle mesh Ewald method[42,43] with a grid spacing of 1.0 Å. Short-range van der Waals and electrostatic interactions were calculated using a cutoff of 9 Å with a switching function applied beyond 8 Å. Multiple time step integration was applied[52] with timesteps of 4 fs for long-range electrostatic forces, 2 fs for short-range nonbonded forces, and 2 fs for bonded forces.

We used the same configuration of the equilibrated bilayer to prepare the three separate systems for GBI1, GBI2, and GBIC. We used the force fields for GBI1 and GBI2 from our previous relative binding free energies study.[36] GBIC was parametrized in a similar manner as previously described for 2GBI.[36] The CHARMM generalized force field parameters were obtained from the ParamChem server, https://cgenff.umaryland.edu/[53,54] We compared the energy minimized structure from the force field with that of a gas phase MP2/6–31G* geometry optimization to ensure that we had comparable minimum energy structures. We also assessed the torsional energy profiles and refined dihedral parameters to yield more consistent results with quantum mechanical data (refined parameters in Supporting Information). Each solute was added into the bulk solvent, and we equilibrated the system for an additional 10 ns, maintaining the same MD simulation parameters.

We then performed MD simulations with the adaptive biasing force (ABF) method[32,33] in NAMD. Using the colvars[55] module in NAMD, we defined a one-dimensional collective variable (denoted as *z*) to describe the relative position of the solute along the transmembrane axis, specified as the center of mass position of the solute relative to the center of mass position of the carbonyl carbon atoms of the POPC molecules. The collective variable was stratified into eleven overlapping windows whose boundaries are listed in Table 1 and depicted at the bottom of Figure 2. The window boundaries were maintained using harmonic restraints with force constants of 10 kcal/mol/Å^2. The forces applied by ABF were collected with a bin width of 0.1 Å. A total of 1000 samples were collected per bin prior to application of ABF to avoid nonequilibrium effects in system dynamics. Each window was sampled separately for each permeant, at a minimum of 40 ns per window per permeant. The windows comprising the collective variable in bulk water (labeled 01,...,11

in Table 1) were initiated from equilibrated MD simulations, and each subsequent window approaching the center of the bilayer was initiated from the previous overlapping window. Window 06 (*cf.* Table 1)was sampled in duplicate, bidirectionally initiated from window 05 and window 07. Convergence was reached more quickly for windows in which the solute was only in bulk water ($|z| = 30$ to 40 Å). Convergence took longer in both inhomogeneous environments (e.g., membrane headgroups) as well as in the hydrophobic interior of the membrane. The minimum, total amount of simulation time for each solute was at least 1 µs. For all molecules in aggregate, we simulated a total of 6.7µs.

One of the key events of membrane permeation is solute "flip-flop" across the hydrophobic membrane core.[28] This flip-flop may occur over long timescales,[56] preventing adequate sampling of the interior hydrophobic region of the membrane (see also the example in Supporting Information). For this reason, we employed a bidirectional approach following the protocol of Li et al.[57] to compute membrane permeation, with the solute approaching the membrane center from both the upper and lower leaflets of the bilayer. For each leaflet of the membrane, we combined the gradients obtained from ABF simulations over successive windows by averaging the overlapping gradients between neighboring windows. The combined gradient data for each leaflet was integrated to yield the PMF corresponding to each half of the membrane. The PMFs were shifted such that the average value in bulk water ($|z| = 35$ to 40 Å) is equal to zero kcal/mol. The upper and lower leaflet PMFs were then combined under the assumption that the solute interacts strongly with only one leaflet at a time, leading to independent contributions to the overall PMF at given value of the collective variable. The resulting PMF is given by[57]

$$W(z) = -k_B T \ln\left\{ e^{-W_{\text{upper}}(z)/k_B T} + e^{-W_{\text{lower}}(z)/k_B T} \right\}. \qquad (2)$$

Noting the symmetry of the bilayer, we symmetrized the resulting PMF by averaging about the bilayer center. Error bars were estimated as the difference between the unsymmetrized and symmetrized PMFs.[35]

Finally, from the potential of mean force $W(z)$, we computed the free energy difference for the small molecule to partition into the membrane from bulk water using the equation:[58–60]

$$\Delta G(\text{wat} \rightarrow \text{mem}) = -k_B T \ln\left\{ \frac{1}{z_2 - z_1} \int_{z_1}^{z_2} e^{-\frac{W(z) - W(z_1)}{k_B T}} \, dz \right\}, \qquad (3)$$

where z_1 and z_2 represent points in bulk water on opposite sides of the membrane. In general terms, the transfer free energy of a solute from one solvent to another is proportional to the log of the partition coefficient, that is, $\Delta G(z) = -k_B T \ln K(z)$. The partition coefficient, $K(z)$, is a form of equilibrium constant describing the ratio of the concentrations of the solute in each solvent,[61–63] where the two solvents here are the aqueous phase regions on opposite sides of the membrane. We do not simulate these concentrations directly but determine this equilibrium constant from integrating the exponential of the Boltzmann-weighted free energy (PMF) along this coordinate. Error bars were estimated by propagating[64] the uncertainty values of the PMFs.

Results and Discussion

In this work, we used atomistic MD simulations with ABF to compute the free energy profiles (or PMFs) for various Hv1 inhibitors to permeate a lipid bilayer (Figure 2). We rationalize the apparent increased ability of 5-chloro-2-guanidinobenzimidazole (GBIC) to permeate the membrane, in contrast to 2-guanidinobenzimidazole (2GBI), primarily based on its energetically favorable state in the membrane interior.

The PMFs for membrane permeation of 2GBI tautomer 1 (GBI1), 2GBI tautomer 2 (GBI2), and GBIC are presented in Figure 3. Comparing the bilayer center ($z = 0$ Å) to bulk water ($z = 30$ Å), the two tautomers of 2GBI have highly similar PMFs, with GBI2 having a slightly higher barrier than GBI1. The profile for GBIC, in contrast, reveals more favorable energetics to membrane permeation. Comparing the barrier height energy differences of the PMFs from the minimum to the maximum of the potentials, the results are (9.3 ± 0.4 kcal/mol) GBI1, (10.9 ± 0.5 kcal/mol) GBI2, and (6.8 ± 0.7 kcal/mol) GBIC. The PMFs show that the most energetically favorable position for the solute in the bilayer is generally in the range of $|z| = 15 - 20$ Å, which corresponds to the POPC lipid headgroup regions, including the negatively charged phosphate groups (Figure 2).

We also computed the water-membrane partitioning free energies by integrating the Boltzmann-weighted PMFs (equation 3). These values, shown in Table 2, suggest a greater likelihood for GBIC to partition into the membrane compared to GBI1 and GBI2. MD simulations based on the inhomogeneous solubility-diffusion model have previously been found to consistently overestimate permeability values relative to experimental values,[34] so we do not propose our results to be quantitative estimates of membrane permeation. Complicating factors include membrane composition, subdiffusive behavior, insufficient sampling, and force field accuracy.[34,35,65–69] The substantially lower barrier to membrane crossing for GBIC compared to 2GBI suggests that GBIC would be capable of crossing the membrane faster than 2GBI, assuming that the diffusivity profiles of GBIC and 2GBI are similar.

Due to interactions with the membrane, a translocating molecule may influence the structure of its local environment in the lipid bilayer, potentially leading to membrane deformation.[56,68,70–73] To obtain a general sense of how the the bilayer is affected by a permeating solute, we used the VMD PMEpot plugin[74] to calculate the electrostatic potential of the whole system (Figure 4). The electrostatic potential, measured relative to the bulk water, was averaged over configuration snapshots in which the solute was located at the center of the membrane ($|z| \leq 1$ Å). Panels A–C of Figure 4 show a considerable amount of membrane distortion effects to a similar degree among GBI1, GBI2, and GBIC. Panel D shows a reference electrostatic potential plot of the membrane with the solute in bulk water without influence on the membrane structure. Panel E depicts a representative snapshot from MD simulations in which the solute GBI2 remains coordinated with the membrane and solvated by water molecules as it permeates to the hydrophobic bilayer interior. These guanidine derivatives are positively charged and are able to interact with the negatively charged phosphate groups of the POPC lipid molecules. Electrostatic interactions appear to

be the driving force of membrane deformation, although it has been previously noted that even a permeating water molecule can cause distortion of the bilayer.[72]

To gain a more specific understanding of solute interactions as it translocates across the bilayer, we computed the average number of hydrogen bond configurations as a function of distance from the membrane center (Figure 5). Error bars denote standard deviations. These results reveal that, at the bilayer center, GBI2, and to a lesser extent GBI1, forms a greater number of hydrogen bonding interactions with water compared to GBIC (compare the isodensity surfaces representing the solvation shell structures at the bottom of Figure 5). Concurrent with inducing membrane deformation, a charged solute in the bilayer will also tend to be coordinated by water molecules.[58,73,75–77] The higher average number of hydrogen bond configurations towards the center of the bilayer for GBI2 compared to GBIC may be correlated with the somewhat sharper membrane deformation of GBI2 as evidenced in the electrostatic potential plots.

Also notable in Figure 5 is that GBIC has the highest average number of hydrogen bonding interactions with POPC phosphate groups within 20 Å of the bilayer center (see also solvation shell structure of GBIC). Both GBI1 and GBIC have a more concentrated charge region in the peripheral guanidine moiety (Figure 1), which likely interacts more with the negatively charged phosphate groups. However, GBI1 does not have the same level of interactions to the phosphate groups as GBIC. We hypothesized that the increased interactions of GBIC with with phosphate may be influenced by the dispersion interactions of its chlorine atom with the POPC hydrocarbon tails, leading to a stronger directional preference of the solute relative to the bilayer. We next turn our focus to orientational preferences of each solute as they translocate the lipid bilayer.

To evaluate the solute orientation along the transmembrane direction, we use a vector whose origin is one of the two distal carbon atoms on the benzyl moiety and whose endpoint is the nitrogen atom that bridges the imidazole and guanidine moieties (see Figure 6). The cosine similarity between this vector and the transmembrane direction was evaluated in each of the simulation windows, and and the corresponding distributions are shown in Figure 6. The symmetry of the bilayer leads to antisymmetric orientation results for the solute, so we combined the upper and lower leaflet data by taking the negative of the cosine similarity measures of the lower leaflet.

The top row of Figure 6 shows uniform distributions from −1 (guanidine pointing towards bilayer center) to +1 (guanidine pointing away from bilayer center), indicating that molecules in bulk water have no orientational preference as they are in an isotropic medium. As the solute approaches the bilayer (row 2 of Figure 6), there are marginally higher counts towards the −1 direction. This is in the region in which the solute begins to approach the lipid headgroups (Figure 2) and will likely orient such that the guanidine interacts with the headgroups upon initially partitioning. This seems to be emphasized in the $|z| = 16 - 26$ Å region. At some point, the molecule reorients, flipping around such that as it permeates to the interior of the membrane beyond the headgroups, its positively charged regions can interact with the negatively charged phosphates, while the more hydrophobic benzyl moiety is solvated by the lipid hydrocarbon chains (rows 4–6 of Figure 6). The orientational

preference is weaker for GBI2, possibly due to greater solvation by surrounding water molecules towards the membrane center (Figure 5). On the other hand, GBI1 or GBIC with a more positively charged guanidine tail (as opposed to a more positively charged imidazole center) is more likely to assume configurations in which the guanidine region points out away from the bilayer center and the benzyl moiety is solvated by the hydrophobic lipid tails. Between GBI1 and GBIC which are nearly identical save for the chlorine atom of GBIC, GBIC has a much stronger orientation bias with its guanidine moiety pointing towards bulk water away from the hydrophobic interior.

To explain this stronger orientation preference of GBIC, we contrasted the specific environment around GBIC with that of GBI1. It appears that the molecular size and composition of GBIC is such that the solute can both interact with the negatively charged POPC phosphate groups with its guanidine moiety while also forming dispersion interactions with the hydrocarbon chains with its chlorobenzyl moiety (Figure 7). Interatomic dispersion forces generally increase with the number of electrons, and a chlorine atom would therefore have significantly more dispersion contributions compared to a hydrogen atom. This atomic substitution seems to explain the strong orientational preference of GBIC in the membrane headgroups, as it can be energetically stabilized by dispersion interactions of the chlorobenzyl moiety with the hydrophobic lipid tails in addition to the Coulombic interactions of its guanidine moiety with the lipid phosphate groups.

Finally, it is possible that 2GBI and GBIC do not remain in their protonated forms from bulk water to the varied environments along the transmembrane direction. To estimate whether the molecules will remain protonated as they permeate the bilayer, we computed the pK_a shift profile using the method of Li et al.[57] for 2GBI to analyze the effect of the inhomogeneous environment on the molecule's pK_a (see details in Supporting Information). The pK_a of neutral 2GBI has been experimentally determined to be 7.09.[78] The pK_a of positively charged 2GBI, whether GBI1 or GBI2, is necessarily greater than 7.09. Based on the pK_a shift profile, the pK_a is expected to change by up to +2 pK units. This means that the effect of the membrane will likely lead to an increase in pK_a of positively charged 2GBI to at least 9. This means that GBI1/GBI2 is predicted to exhibit more basic character as it permeates the membrane, particularly in the glycerol-phosphate region, and therefore we do not expect deprotonation during membrane permeation. This is consistent with our observations that 2GBI charge moieties retain a polar solvation shell trough the entire membrane region (Figure 5). As a point of reference, even a positively charged arginine residue is predicted to remain 70–99% protonated while partitioning into a dipalmitoylphosphatidylcholine (DPPC) lipid bilayer at neutral pH[57] and indeed also remains charged in other diverse environments.[79–81]

Conclusions

In this work, we computed PMFs to estimate the relative energetic barriers for two Hv1 channel blockers to permeate the membrane. Experimental evidence suggests that GBIC can permeate the membrane and block the channel when added to the extracellular medium.[27] Our results to show that it is much more energetically favorable for GBIC to permeate compared to 2GBI, which is in line with a body of existing literature of experiments and

computations demonstrating that halogen atoms tend to increase the membrane permeability between similar chemical compounds.[82–86] We posit that this trend may be rationalized by considerable stabilization of GBIC vs. 2GBI in the membrane headgroups by both electrostatic and dispersion interactions. Future studies that explore the kinetic contributions to membrane permeability may provide further insight into the cell-absorption propensities of these Hv1 blockers.

Supplementary Material

Refer to Web version on PubMed Central for supplementary material.

Acknowledgement

References

(1). DeCoursey TE Voltage-Gated Proton Channels: Molecular Biology, Physiology, and Pathophysiology of the HV Family. Physiol. Rev 2013, 93, 599–652. [PubMed: 23589829]

(2). Ramsey IS; Moran MM; Chong JA; Clapham DE A Voltage-Gated Proton-Selective Channel Lacking the Pore Domain. Nature 2006, 440, 1213–1216. [PubMed: 16554753]

(3). Sasaki M; Takagi M; Okamura Y A Voltage Sensor-Domain Protein Is a Voltage-Gated Proton Channel. Science 2006, 312, 589–592. [PubMed: 16556803]

(4). Ramsey IS; Mokrab Y; Carvacho I; Sands ZA; Sansom MSP; Clapham DE An Aqueous H + Permeation Pathway in the Voltage-Gated Proton Channel Hv1. Nat. Struct. Mol. Biol 2010, 17, 869–875. [PubMed: 20543828]

(5). Koch HP; Kurokawa T; Okochi Y; Sasaki M; Okamura Y; Larsson HP Multimeric Nature of Voltage-Gated Proton Channels. Proc. Acad. Natl. Sci. U. S. A 2008, 105, 9111–9116.

(6). Lee S-Y; Letts JA; MacKinnon R Dimeric Subunit Stoichiometry of the Human Voltage-Dependent Proton Channel Hv1. Proc. Acad. Natl. Sci. U. S. A 2008, 105, 7692–7695.

(7). Tombola F; Ulbrich MH; Isacoff EY The Voltage-Gated Proton Channel Hv1 Has Two Pores, Each Controlled by One Voltage Sensor. Neuron 2008, 58, 546–556. [PubMed: 18498736]

(8). Musset B; Smith SME; Rajan S; Morgan D; Cherny VV; DeCoursey TE Aspartate 112 Is the Selectivity Filter of the Human Voltage-Gated Proton Channel. Nature 2011, 480, 273–277. [PubMed: 22020278]

(9). Berger TK; Isacoff EY The Pore of the Voltage-Gated Proton Channel. Neuron 2011, 72, 991–1000. [PubMed: 22196334]

(10). Takeshita K; Sakata S; Yamashita E; Fujiwara Y; Kawanabe A; Kurokawa T; Okochi Y; Matsuda M; Narita H; Okamura Y; Nakagawa A X-Ray Crystal Structure of Voltage-Gated Proton Channel. Nat. Struct. Mol. Biol 2014, 21, 352–357. [PubMed: 24584463]

(11). El Chemaly A; Okochi Y; Sasaki M; Arnaudeau S; Okamura Y; Demaurex N VSOP/Hv1 Proton Channels Sustain Calcium Entry, Neutrophil Migration, and Superoxide Production by Limiting Cell Depolarization and Acidification. J. Exp. Med 2010, 207, 129–139. [PubMed: 20026664]

(12). DeCoursey TE; Morgan D; Cherny VV The Voltage Dependence of NADPH Oxidase Reveals Why Phagocytes Need Proton Channels. Nature 2003, 422, 531–534. [PubMed: 12673252]

(13). Morgan D; Capasso M; Musset B; Cherny VV; Ríos E; Dyer MJS; DeCoursey TE Voltage-Gated Proton Channels Maintain pH in Human Neutrophils during Phagocytosis. Proc. Acad. Natl. Sci. U. S. A 2009, 106, 18022–18027.

(14). Okochi Y; Sasaki M; Iwasaki H; Okamura Y Voltage-Gated Proton Channel Is Expressed on Phagosomes. Biochem. Biophys. Res. Commun 2009, 382, 274–279. [PubMed: 19285483]

(15). Ramsey IS; Ruchti E; Kaczmarek JS; Clapham DE Hv1 Proton Channels Are Required for High-Level NADPH Oxidase-Dependent Superoxide Production during the Phagocyte Respiratory Burst. Proc. Acad. Natl. Sci. U. S. A 2009, 106, 7642–7647.

(16). Seredenina T; Demaurex N; Krause K-H Voltage-Gated Proton Channels as Novel Drug Targets: From NADPH Oxidase Regulation to Sperm Biology. Antioxid. Redox Signal. 2014, 23, 490–513. [PubMed: 24483328]

(17). Musset B; Morgan D; Cherny VV; MacGlashan DW; Thomas LL; Ríos E; DeCoursey TE A pH-Stabilizing Role of Voltage-Gated Proton Channels in IgE-Mediated Activation of Human Basophils. Proc. Acad. Natl. Sci. U. S. A 2008, 105, 11020–11025.

(18). Zhu X; Mose E; Zimmermann N Proton Channel HVCN1 Is Required for Effector Functions of Mouse Eosinophils. BMC Immunology 2013, 14, 24. [PubMed: 23705768]

(19). Wang Y; Li SJ; Pan J; Che Y; Yin J; Zhao Q Specific Expression of the Human Voltage-Gated Proton Channel Hv1 in Highly Metastatic Breast Cancer Cells, Promotes Tumor Progression and Metastasis. Biochem. Biophys. Res. Commun 2011, 412, 353–359. [PubMed: 21821008]

(20). Wang Y; Li SJ; Wu X; Che Y; Li Q Clinicopathological and Biological Significance of Human Voltage-Gated Proton Channel Hv1 Protein Overexpression in Breast Cancer. J. Biol. Chem 2012, 287, 13877–13888.

(21). Hondares E; Brown MA; Musset B; Morgan D; Cherny VV; Taubert C; Bhamrah MK; Coe D; Marelli-Berg F; Gribben JG; Dyer MJS; DeCoursey TE; Capasso M Enhanced Activation of an Amino-Terminally Truncated Isoform of the Voltage-Gated Proton Channel HVCN1 Enriched in Malignant B Cells. Proc. Acad. Natl. Sci. U. S. A 2014, 111, 18078–18083.

(22). Ventura C; Leon IE; Asuaje A; Martín P; Enrique N; Núñez M; Cocca C; Milesi V Differential Expression of the Long and Truncated Hv1 Isoforms in Breast-Cancer Cells. J. Cell. Physiol 2020,

(23). Wu L-J; Wu G; Sharif MRA; Baker A; Jia Y; Fahey FH; Luo HR; Feener EP; Clapham DE The Voltage-Gated Proton Channel Hv1 Enhances Brain Damage from Ischemic Stroke. Nat. Neurosci 2012, 15, 565–573. [PubMed: 22388960]

(24). Kawai T; Okochi Y; Ozaki T; Imura Y; Koizumi S; Yamazaki M; Abe M; Sakimura K; Yamashita T; Okamura Y Unconventional Role of Voltage-Gated Proton Channels (VSOP/Hv1) in Regulation of Microglial ROS Production. J. Neurochem 2017, 142, 686–699. [PubMed: 28628214]

(25). Li W; Ward R; Dong G; Ergul A; O'Connor P Neurovascular Protection in Voltage-Gated Proton Channel Hv1 Knock-out Rats after Ischemic Stroke: Interaction with Na+/H+ Exchanger-1 Antagonism. Physiol. Rep 2019, 7, e14142.

(26). Hong L; Pathak MM; Kim IH; Ta D; Tombola F Voltage-Sensing Domain of Voltage-Gated Proton Channel Hv1 Shares Mechanism of Block with Pore Domains. Neuron 2013, 77, 274–287. [PubMed: 23352164]

(27). Hong L; Kim IH; Tombola F Molecular Determinants of Hv1 Proton Channel Inhibition by Guanidine Derivatives. Proc. Natl. Acad. Sci. U. S. A 2014, 111, 9971. [PubMed: 24912149]

(28). Dickson CJ; Hornak V; Pearlstein RA; Duca JS Structure–Kinetic Relationships of Passive Membrane Permeation from Multiscale Modeling. J. Am. Chem. Soc 2017, 139, 442–452. [PubMed: 27951634]

(29). Diamond JM; Katz Y Interpretation of Nonelectrolyte Partition Coefficients between Dimyristoyl Lecithin and Water. J. Membrain Biol 1974, 17, 121–154.

(30). Marrink S-J; Berendsen HJC Simulation of Water Transport through a Lipid Membrane. J. Phys. Chem 1994, 98, 4155–4168.

(31). Parisio G; Stocchero M; Ferrarini A Passive Membrane Permeability: Beyond the Standard Solubility-Diffusion Model. J. Chem. Theory Comput 2013, 9, 5236–5246. [PubMed: 26592263]

(32). Darve E; Rodríguez-Gómez D; Pohorille A Adaptive Biasing Force Method for Scalar and Vector Free Energy Calculations. J. Chem. Phys 2008, 128, 144120.

(33). Hénin J; Fiorin G; Chipot C; Klein ML Exploring Multidimensional Free Energy Landscapes Using Time-Dependent Biases on Collective Variables. J. Chem. Theory Comput 2010, 6, 35–47. [PubMed: 26614317]

(34). Lee CT; Comer J; Herndon C; Leung N; Pavlova A; Swift RV; Tung C; Rowley CN; Amaro RE; Chipot C; Wang Y; Gumbart JC Simulation-Based Approaches for Determining Membrane Permeability of Small Compounds. J. Chem. Inf. Model 2016, 56, 721–733. [PubMed: 27043429]

(35). Tse CH; Comer J; Wang Y; Chipot C Link between Membrane Composition and Permeability to Drugs. J. Chem. Theory Comput 2018, 14, 2895–2909. [PubMed: 29771515]

(36). Lim VT; Geragotelis AD; Lim NM; Freites JA; Tombola F; Mobley DM; Tobias DJ Insights on small molecule binding to the Hv1 proton channel from free energy calculations with molecular dynamics simulations. Scientific Reports 2020,

(37). Klauda JB; Venable RM; Freites JA; O'Connor JW; Tobias DJ; Mondragon-Ramirez C; Vorobyov I; MacKerell AD; Pastor RW Update of the CHARMM All-Atom Additive Force Field for Lipids: Validation on Six Lipid Types. J. Phys. Chem. B 2010, 114, 7830–7843. [PubMed: 20496934]

(38). Jorgensen WL; Chandrasekhar J; Madura JD; Impey RW; Klein ML Comparison of Simple Potential Functions for Simulating Liquid Water. J. Chem. Phys 1983, 79, 926–935.

(39). MacKerell AD et al. All-Atom Empirical Potential for Molecular Modeling and Dynamics Studies of Proteins. J. Phys. Chem. B 1998, 102, 3586–3616. [PubMed: 24889800]

(40). Bowers KJ; Chow DE; Xu H; Dror RO; Eastwood MP; Gregersen BA; Klepeis JL; Kolossvary I; Moraes MA; Sacerdoti FD; Salmon JK; Shan Y; Shaw DE Scalable Algorithms for Molecular Dynamics Simulations on Commodity Clusters. SC '06: Proceedings of the 2006 ACM/IEEE Conference on Supercomputing. 2006; pp 43–43.

(41). Tuckerman M; Berne BJ; Martyna GJ Reversible Multiple Time Scale Molecular Dynamics. J. Chem. Phys 1992, 97, 1990–2001.

(42). Darden T; York D; Pedersen L Particle Mesh Ewald: An N·log(N) Method for Ewald Sums in Large Systems. J. Chem. Phys 1993, 98, 10089–10092.

(43). Essmann U; Perera L; Berkowitz ML; Darden T; Lee H; Pedersen LG A Smooth Particle Mesh Ewald Method. J. Chem. Phys 1995, 103, 8577–8593.

(44). Ryckaert J-P; Ciccotti G; Berendsen HJC Numerical Integration of the Cartesian Equations of Motion of a System with Constraints: Molecular Dynamics of n-Alkanes. J. Comput. Phys 1977, 23, 327–341.

(45). Martyna GJ; Klein ML; Tuckerman M Nosé–Hoover Chains: The Canonical Ensemble via Continuous Dynamics. J. Chem. Phys 1992, 97, 2635–2643.

(46). Martyna GJ; Tobias DJ; Klein ML Constant Pressure Molecular Dynamics Algorithms. J. Chem. Phys1994, 101, 4177–4189.

(47). Phillips JC; Braun R; Wang W; Gumbart J; Tajkhorshid E; Villa E; Chipot C; Skeel RD; Kalé L; Schulten K Scalable Molecular Dynamics with NAMD. J. Comput. Chem 2005, 26, 1781–1802. [PubMed: 16222654]

(48). Bussi G; Donadio D; Parrinello M Canonical Sampling through Velocity Rescaling. J. Chem. Phys 2007, 126, 014101.

(49). Feller SE; Zhang Y; Pastor RW; Brooks BR Constant Pressure Molecular Dynamics Simulation: The Langevin Piston Method. J. Chem. Phys 1995, 103, 4613–4621.

(50). Miyamoto S; Kollman PA Settle: An Analytical Version of the SHAKE and RATTLE Algorithm for Rigid Water Models. J. Comput. Chem 1992, 13, 952–962.

(51). Andersen HC Rattle: A "Velocity" Version of the Shake Algorithm for Molecular Dynamics Calculations. J. Comput. Phys 1983, 52, 24–34.

(52). Grubmüller H; Heller H; Windemuth A; Schulten K Generalized Verlet Algorithm for Efficient Molecular Dynamics Simulations with Long-Range Interactions. Mol. Simul 1991, 6, 121–142.

(53). Vanommeslaeghe K; MacKerell AD Automation of the CHARMM General Force Field (CGenFF) I: Bond Perception and Atom Typing. J. Chem. Inf. Model 2012, 52, 3144–3154. [PubMed: 23146088]

(54). Vanommeslaeghe K; Raman EP; MacKerell AD Automation of the CHARMM General Force Field (CGenFF) II: Assignment of Bonded Parameters and Partial Atomic Charges. J. Chem. Inf. Model 2012, 52, 3155–3168. [PubMed: 23145473]

(55). Fiorin G; Klein ML; Hénin J Using Collective Variables to Drive Molecular Dynamics Simulations. Mol. Phys 2013, 111, 3345–3362.

(56). Awoonor-Williams E; Rowley CN Molecular Simulation of Nonfacilitated Membrane Permeation. Biochim. Biophys. Acta, Biomembranes 2016, 1858, 1672–1687.

(57). Li L; Vorobyov I; Allen TW Potential of Mean Force and pKa Profile Calculation for a Lipid Membrane-Exposed Arginine Side Chain. J. Phys. Chem. B 2008, 112, 9574–9587. [PubMed: 18636765]

(58). DeMarco KR; Bekker S; Clancy CE; Noskov SY; Vorobyov I Digging into Lipid Membrane Permeation for Cardiac Ion Channel Blocker D-Sotalol with All-Atom Simulations. Front. Pharmacol 2018, 9.

(59). MacCallum JL; Tieleman DP Computer Simulation of the Distribution of Hexane in a Lipid Bilayer: Spatially Resolved Free Energy, Entropy, and Enthalpy Profiles. J. Am. Chem. Soc 2006, 128, 125–130. [PubMed: 16390139]

(60). Vorobyov I; Bennett WD; Tieleman DP; Allen TW; Noskov S The Role of Atomic Polarization in the Thermodynamics of Chloroform Partitioning to Lipid Bilayers. J. Chem. Theory Comput 2012, 8, 618–628. [PubMed: 26596610]

(61). Vivcharuk V; Kaznessis YN Thermodynamic Analysis of Protegrin-1 Insertion and Permeation through a Lipid Bilayer. J. Phys. Chem. B 2011, 115, 14704–14712.

(62). Hossain S; Kabedev A; Parrow A; Bergström CAS.; Larsson P Molecular Simulation as a Computational Pharmaceutics Tool to Predict Drug Solubility, Solubilization Processes and Partitioning. European Journal of Pharmaceutics and Biopharmaceutics 2019, 137, 46–55. [PubMed: 30771454]

(63). Bannan CC; Calabró G; Kyu DY; Mobley DL Calculating Partition Coefficients of Small Molecules in Octanol/Water and Cyclohexane/Water. J. Chem. Theory Comput 2016, 12, 4015–4024. [PubMed: 27434695]

(64). Lebigot EO Uncertainties: a Python package for calculations with uncertainties. URL http://pythonhostedorg/uncertainties 2010,

(65). Comer J; Schulten K; Chipot C Permeability of a Fluid Lipid Bilayer to Short-Chain Alcohols from First Principles. J. Chem. Theory Comput 2017, 13, 2523–2532. [PubMed: 28475319]

(66). Rivel T; Ramseyer C; Yesylevskyy S The Asymmetry of Plasma Membranes and Their Cholesterol Content Influence the Uptake of Cisplatin. Sci. Rep 2019, 9, 1–14. [PubMed: 30626917]

(67). Ly HV; Longo ML The Influence of Short-Chain Alcohols on Interfacial Tension, Mechanical Properties, Area/Molecule, and Permeability of Fluid Lipid Bilayers. Biophys. J 2004, 87, 1013–1033. [PubMed: 15298907]

(68). Venable RM; Krämer A; Pastor RW Molecular Dynamics Simulations of Membrane Permeability. Chem. Rev 2019, 119, 5954–5997. [PubMed: 30747524]

(69). Chipot C; Comer J Subdiffusion in Membrane Permeation of Small Molecules. Sci. Rep 2016, 6, 1–14. [PubMed: 28442746]

(70). Gennis RB In Biomembranes: Molecular Structure and Function; Gennis RB, Ed.; Springer Advanced Texts in Chemistry; Springer: New York, NY, 1989; pp 235–269.

(71). Shinoda W Permeability across Lipid Membranes. Biochim. Biophys. Acta, Biomembranes 2016, 1858, 2254–2265.

(72). Comer J; Schulten K; Chipot C Calculation of Lipid-Bilayer Permeabilities Using an Average Force. J. Chem. Theory Comput 2014, 10, 554–564. [PubMed: 26580032]

(73). Schow EV; Freites JA; Cheng P; Bernsel A; von Heijne G; White SH; Tobias DJ Arginine in Membranes: The Connection Between Molecular Dynamics Simulations and Translocon-Mediated Insertion Experiments. J. Membr. Biol 2011, 239, 35–48. [PubMed: 21127848]

(74). Aksimentiev A; Schulten K Imaging a-Hemolysin with Molecular Dynamics: Ionic Conductance, Osmotic Permeability, and the Electrostatic Potential Map. Biophys. J 2005, 88, 3745–3761. [PubMed: 15764651]

(75). Vorobyov I; Olson TE; Kim JH; Koeppe RE; Andersen OS; Allen TW Ion-Induced Defect Permeation of Lipid Membranes. Biophys. J 2014, 106, 586–597. [PubMed: 24507599]

(76). Dorairaj S; Allen TW On the Thermodynamic Stability of a Charged Arginine Side Chain in a Transmembrane Helix. Proc. Acad. Natl. Sci. U. S. A 2007, 104, 4943–4948.

(77). Freites JA; Tobias DJ; von Heijne G; White SH Interface Connections of a Transmembrane Voltage Sensor. Proc. Acad. Natl. Sci. U. S. A 2005, 102, 15059–15064.

(78). Acerete C; Catalan J; Fabero F; Sanchez-Cabezudo M; Maria Claramunt R; Elguero J Structure and Basicity of 2-Guanidiobenzimidazoles. HETEROCYCLES 1987, 26, 1581.

(79). Yoo J; Cui Q Does Arginine Remain Protonated in the Lipid Membrane? Insights from Microscopic pKa Calculations. Biophys. J 2008, 94, L61–L63. [PubMed: 18199662]

(80). Fitch CA; Platzer G; Okon M; E BG-M; McIntosh LP Arginine: Its pKa Value Revisited. Protein Sci. 2015, 24, 752–761. [PubMed: 25808204]

(81). Harms MJ; Schlessman JL; Sue GR; E BG-M. Arginine Residues at Internal Positions in a Protein Are Always Charged. Proc. Acad. Natl. Sci. U. S. A 2011, 108, 18954–18959.

(82). Riley E, K; Hobza PThe Relative Roles of Electrostatics and Dispersion in the Stabilization of Halogen Bonds. Phys. Chem. Chem. Phys 2013, 15, 17742–17751.

(83). Wallnoefer G, H.; Fox T; Liedl R, K.; Tautermann S, C.Dispersion Dominated Halogen–π Interactions: Energies and Locations of Minima. Phys. Chem. Chem. Phys 2010, 12, 14941–14949.

(84). Gentry CL; Egleton RD; Gillespie T; Abbruscato TJ; Bechowski HB; Hruby VJ; Davis TP The Effect of Halogenation on Blood–Brain Barrier Permeability of a Novel Peptide Drug. Peptides 1999, 20, 1229–1238. [PubMed: 10573295]

(85). Gerebtzoff G; Li-Blatter X; Fischer H; Frentzel A; Seelig A Halogenation of Drugs Enhances Membrane Binding and Permeation. ChemBioChem 2004, 5, 676–684. [PubMed: 15122640]

(86). Govindaraj V; Ungati H; Jakka SR; Bose S; Mugesh G Directing Traffic: Halogen-Bond-Mediated Membrane Transport. Chem. Eur. J 2019, 25, 11180–11192.
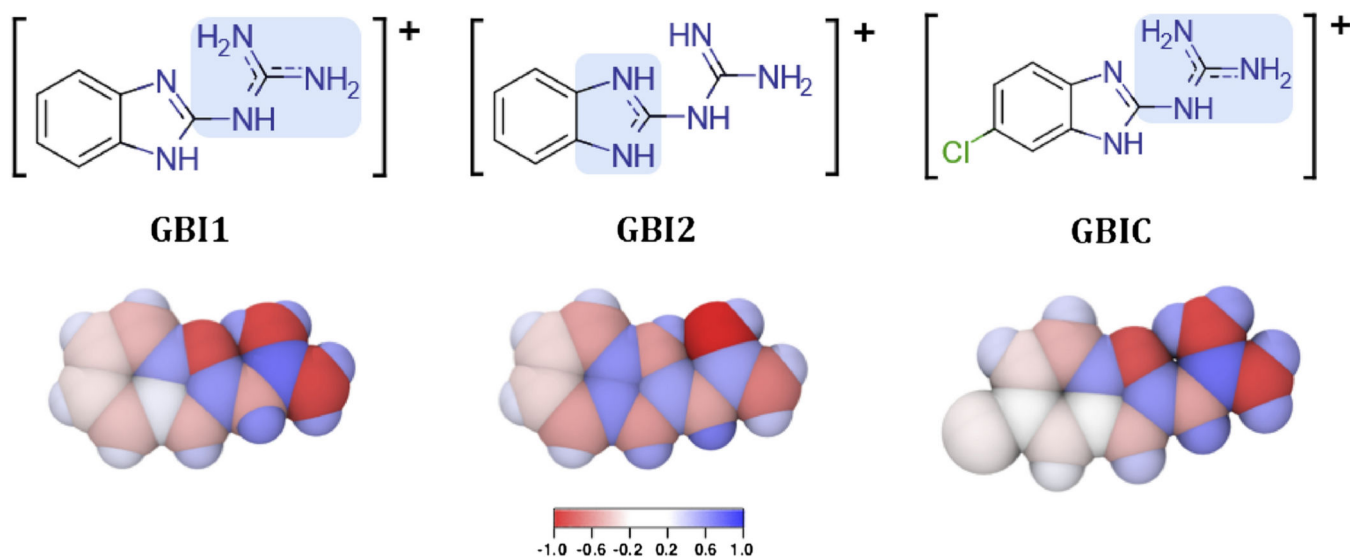
Figure 1:
Chemical structures of molecules in this study. GBI1 and GBI2 refer to distinct tautomeric states of the positively charged molecule, 2-guanidinobenzimidazole. GBIC refers to 5-chloro-2-guanidinobenzimidazole. The shaded blue regions have higher positive charge density. The molecules are also shown as filled-spheres colored by partial charge magnitude (in elementary charge units).
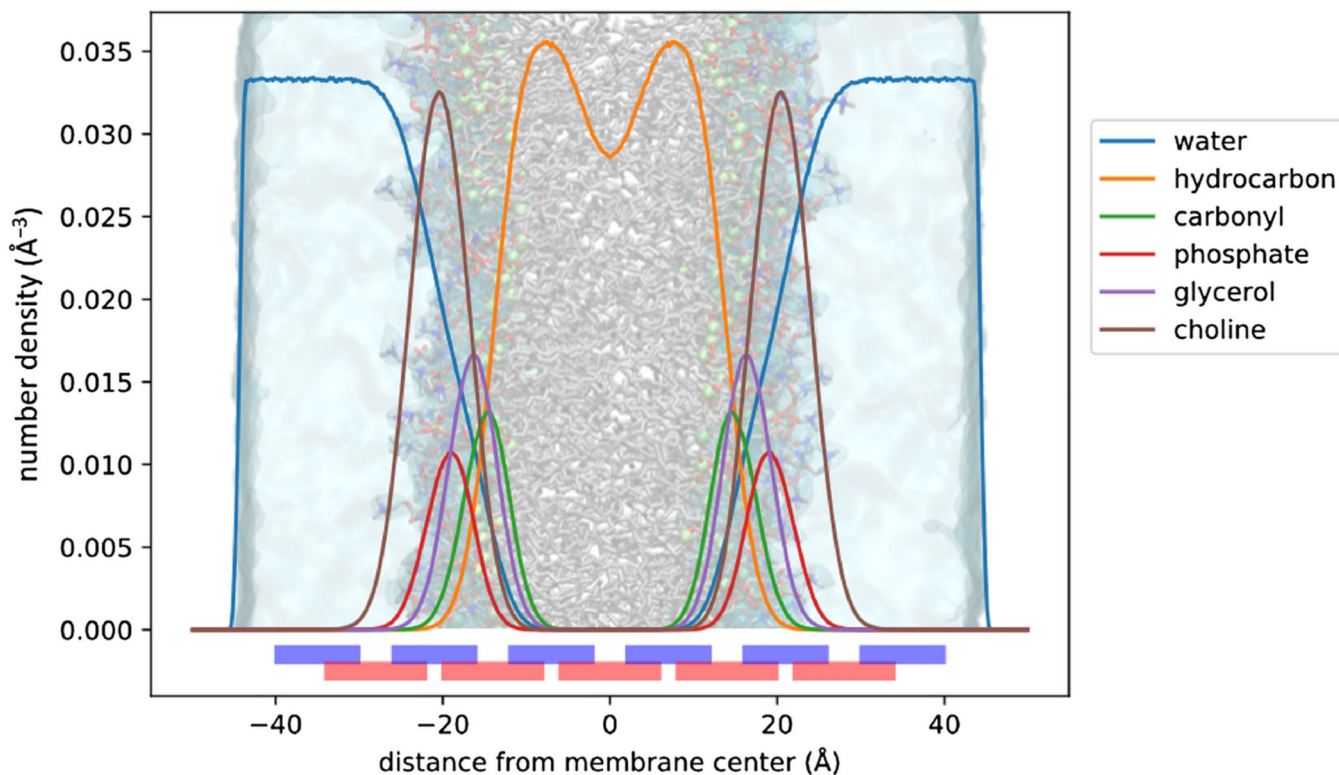
Figure 2:
Number density profiles water molecules and lipid molecule moieties of the hydrated POPC bilayer used in this work. The one-dimensional collective variable for adaptive biasing force simulations is defined as the distance between the z coordinate of the center of mass of the solute to the z coordinate of the center of mass of the carbonyl carbons of the POPC lipids. Waters are drawn in slabs of light blue, and lipids are in licorice representation with their carbonyl carbons shown as green filled spheres. The collective variable is stratified into eleven overlapping windows whose distance boundaries are denoted in the red and blue rectangles and listed in Table 1.
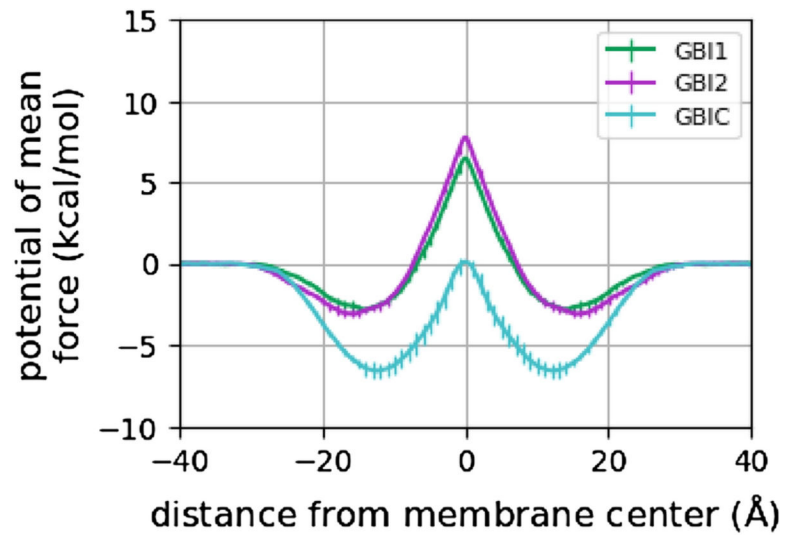
Figure 3:
Symmetrized potentials of mean force of some Hv1 channel blockers to permeate the membrane. Error bars signify deviation from symmetry about the middle of the bilayer at $z = 0$ Å.
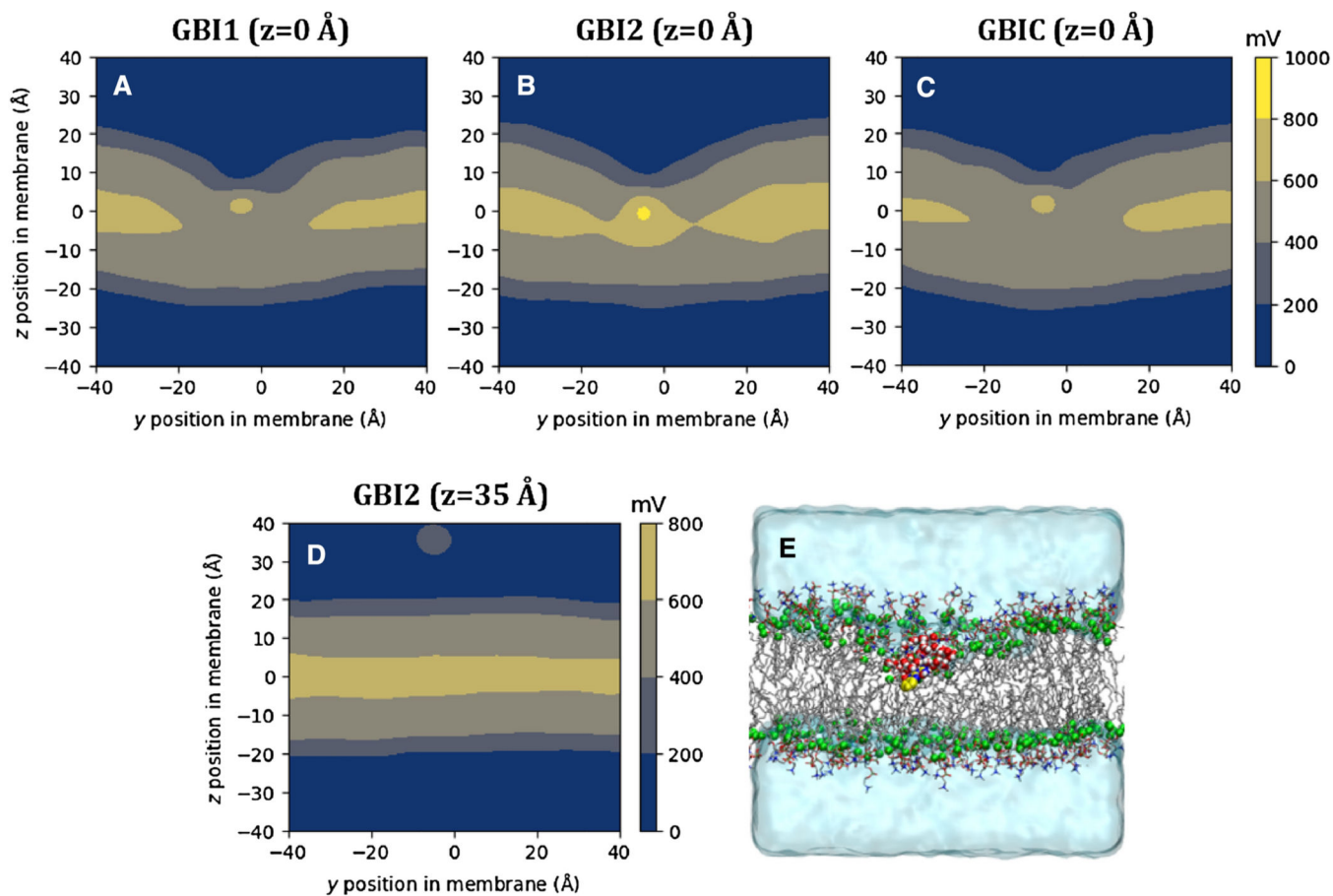
Figure 4:

Contour plots representing the averaged electrostatic potential of the system for when the solute is located at |z| ≤ 1.0 Å. Panels **A**, **B**, and **C** show the system with GBI1, GBI2, and GBIC, respectively. Panel **D** shows a representative plot of the average electrostatic potential when the solute is in bulk water (here, GBI2 at z = 35 Å). Membrane permeation leads to considerable distortion for all molecules. Panel **E** shows a typical configuration snapshot of the membrane system corresponding to GBI2 located at z = 0 Å. Waters are rendered as light blue slabs, and lipids are in licorice representation with their carbonyl carbons shown as green filled-spheres. GBI2 is shown in filled-sphere representation, with carbon atoms in yellow. Water molecules within 8 Å of GBI2 are shown as red (oxygen) and white (hydrogen) filled-spheres.
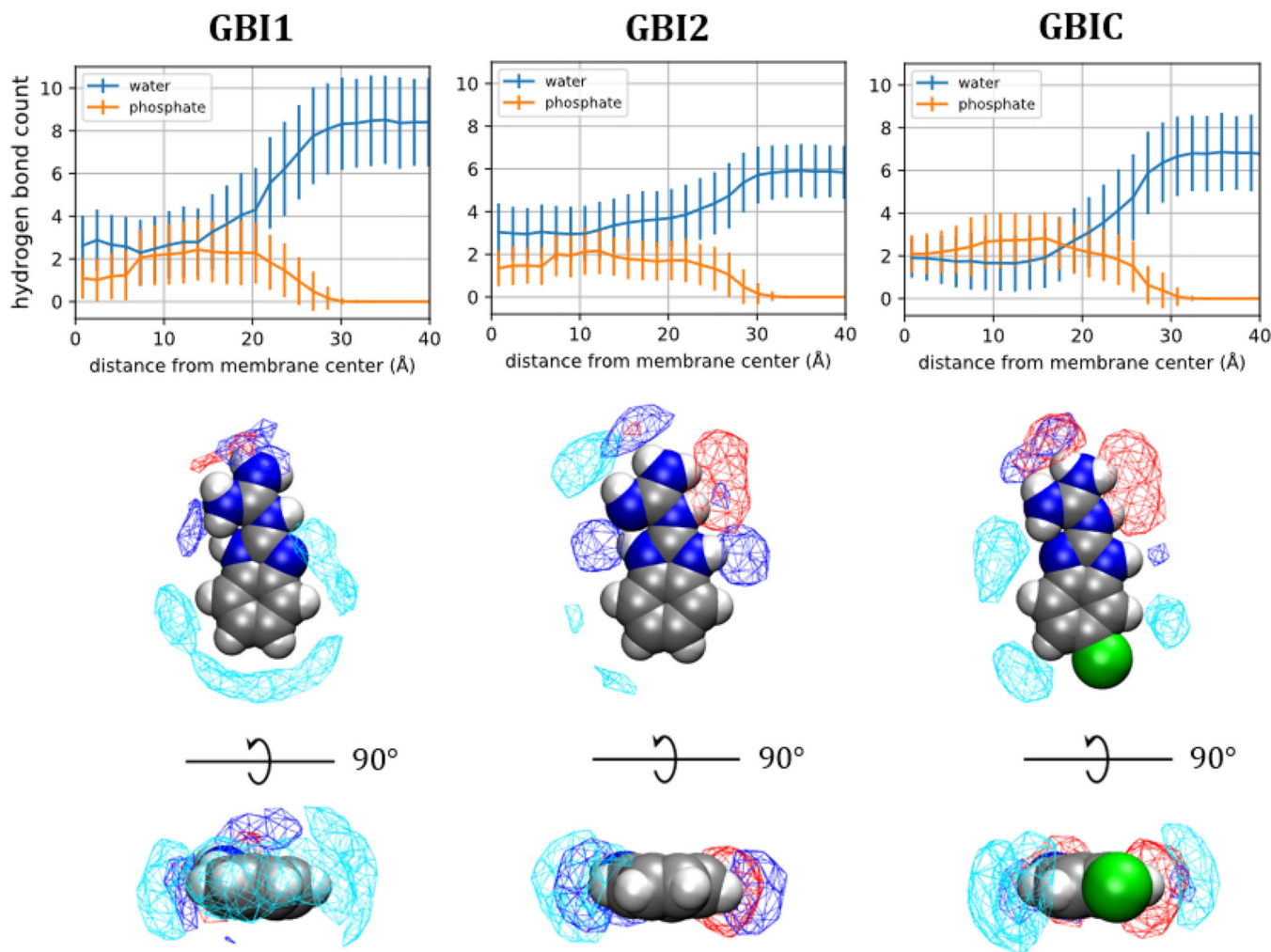
Figure 5:

Top: Average number of hydrogen bonds formed by the solutes with water molecules (blue) and phosphate groups (orange) as a function of the solute center of mass position. Error bars are standard deviations. Hydrogen bonds were calculated using a cutoff distance between donor and acceptor of 3.5 Å and a donor-hydrogen-acceptor cutoff angle of 40°. **Bottom**: Evaluation of the local environment of the solute in the hydrocarbon core region of the membrane ($|z| \leq 1.0$ Å). Solvation shell structures of GBI1, GBI2, and GBIC were computed using spatial distributions of the oxygen atom of water molecules, oxygen atoms of the POPC phosphate groups, and carbon atoms of the POPC hydrocarbon chains. The surfaces represent equal number density for each group: water (blue, 0.013 Å^{-3}), phosphate (red, 0.008 Å^{-3}), and hydrocarbon (cyan, 0.0023 Å^{-3}). The solute is shown in filled-sphere representation colored by atom type (silver, carbon; blue, nitrogen; white, hydrogen; green, chlorine).
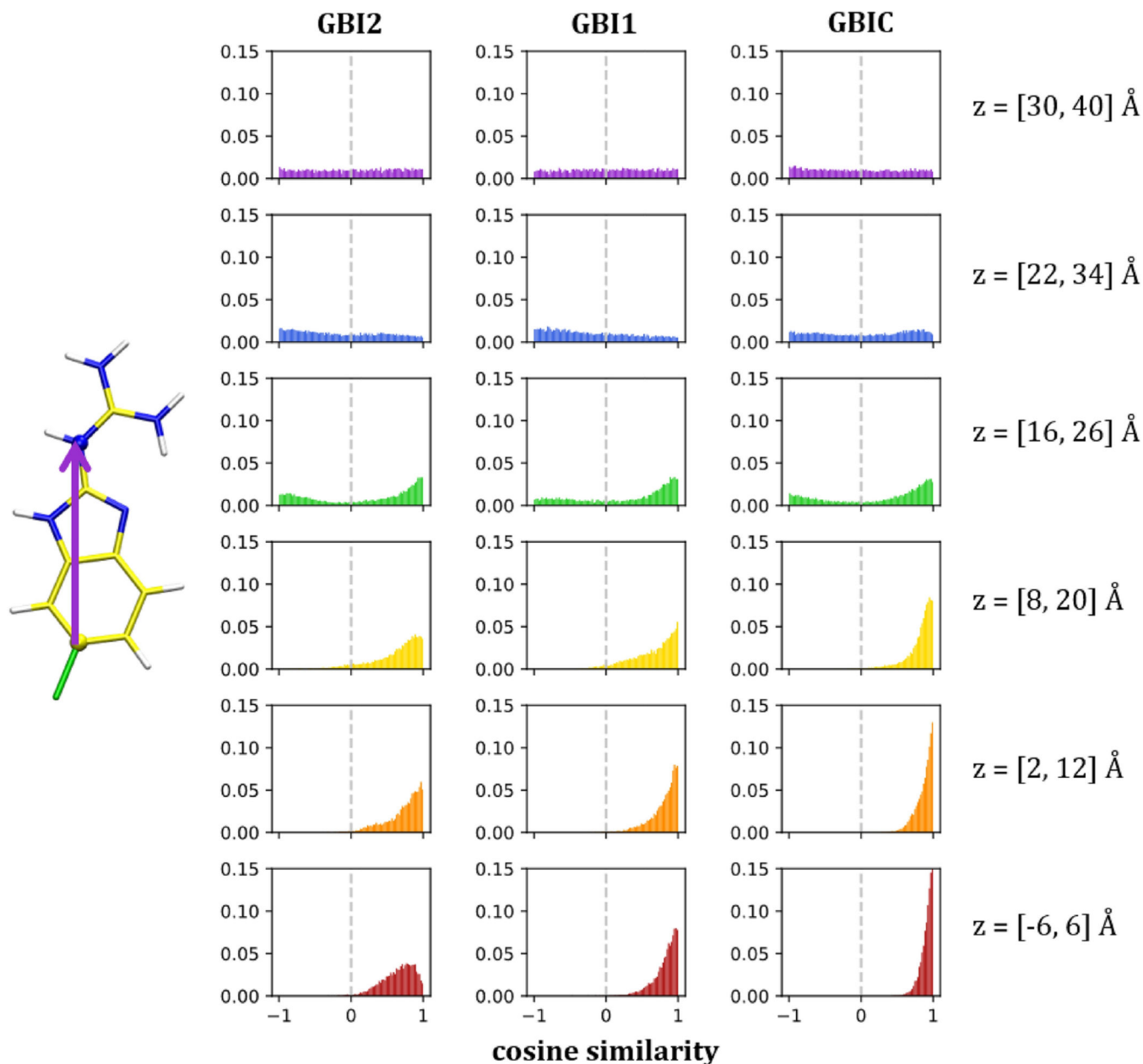
Figure 6:
Probability density histograms of molecule orientation as a function of position along the transmembrane direction (z-axis). A vector is defined using two atoms on the solute (purple arrow). The cosine similarity is computed using this vector and the $+z$ axis to represent the directionality of the solute, wherein a cosine similarity score of 1 means the guanidine moiety is pointing towards $+z$, and a value of -1 means the guanidine moiety is pointing towards $-z$. A cosine similarity of 0 corresponds to the solute oriented perpendicular to the z axis (i.e., parallel to the membrane plane). In this figure, each column shows the histograms for a separate solute, and each row represents a particular range along the collective variable. The symmetry of the upper and lower leaflets of the bilayer results in antisymmetric cosine similarities between the two leaflets (e.g., range [8, 20] Å would be antisymmetric to range

[−20, −8] Å). For each permeant, we take the negative values of the cosine similarity scores of the lower leaflet and histogram them with the cosine similarity scores of the corresponding ranges of the upper leaflet.
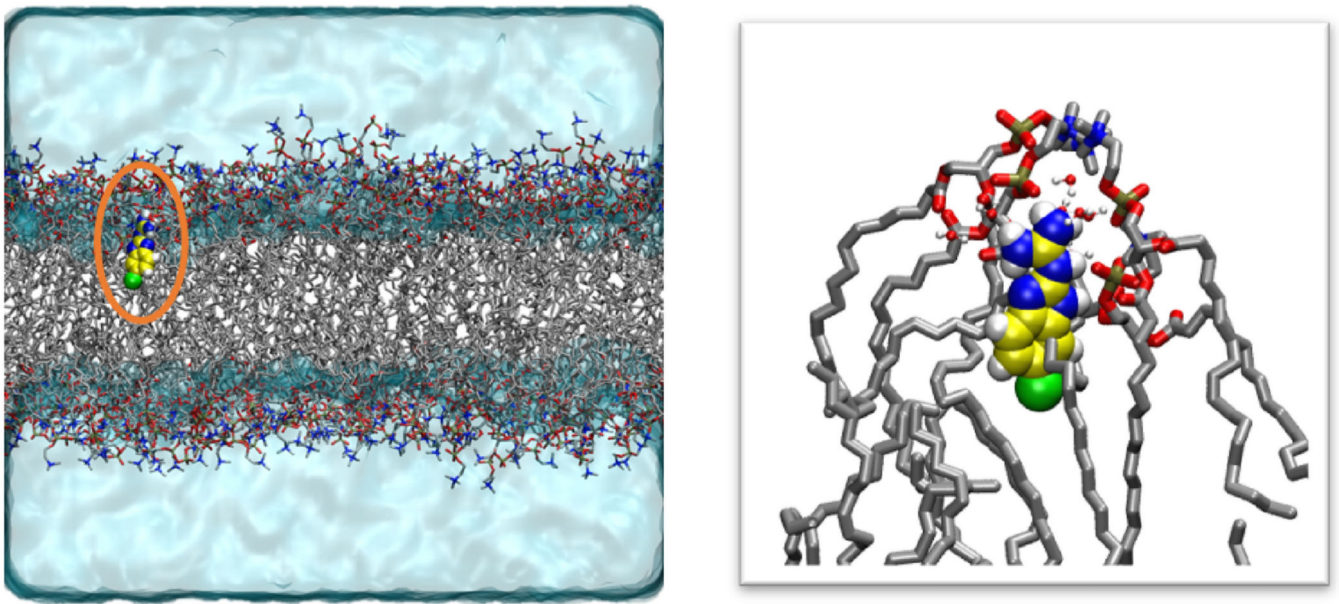
Figure 7:
In addition to electrostatic interactions of the charged guanidine region of the solute with the negative phosphate moieties of POPC, GBIC may be further stabilized by dispersion interactions of its chlorine atom with the hydrocarbon tails of the lipid bilayer. The left panel shows a representative configuration of GBIC in the membrane around the polar/apolar interface ($z = 8$–20 Å). GBIC (circled in orange) is drawn as filled spheres, with carbon atoms in yellow, nitrogen atoms in blue, hydrogen atoms in white, and the chlorine atom in green. The right panel shows a close up view of the local environment around GBIC. Water molecules within 3 Å of the solute are depicted in CPK representation, with farther water and lipid molecules hidden for viewing clarity.

Table 1:

Separation of the collective variable (CV) into windows. The collective variable is defined by the difference of the z coordinate of the permeant center of mass and the z coordinate of the carbonyl carbon atoms of the POPC bilayer.

Window	CV: lower bound (Å)	CV: upper bound (Å)
01	30	40
02	22	34
03	16	26
04	08	20
05	02	12
06	−06	06
07	−12	−02
08	−20	−08
09	−26	−16
10	−34	−22
11	−40	−30

Table 2:

Partitioning free energies estimated from the potentials of mean force. Error bars obtained by propagation of uncertainties.

Permeant	$\Delta G(wat \rightarrow mem)$ (kcal/mol)
GBI1	-1.79 ± 0.02
GBI2	-2.13 ± 0.02
GBIC	-5.49 ± 0.04